

High-flux water desalination with interfacial salt sieving effect in nanoporous carbon composite membranes

Wei Chen^{1,2}, Shuyu Chen³, Tengfei Liang^{3,4}, Qiang Zhang¹, Zhongli Fan¹, Hang Yin¹, Kuo-Wei Huang¹, Xixiang Zhang¹, Zhiping Lai^{1*} and Ping Sheng^{3,5*}

Freshwater flux and energy consumption are two important benchmarks for the membrane desalination process. Here, we show that nanoporous carbon composite membranes, which comprise a layer of porous carbon fibre structures grown on a porous ceramic substrate, can exhibit 100% desalination and a freshwater flux that is 3–20 times higher than existing polymeric membranes. Thermal accounting experiments demonstrated that the carbon composite membrane saved over 80% of the latent heat consumption. Theoretical calculations combined with molecular dynamics simulations revealed the unique microscopic process occurring in the membrane. When the salt solution is stopped at the openings to the nanoscale porous channels and forms a meniscus, the vapour can rapidly transport across the nanoscale gap to condense on the permeate side. This process is driven by the chemical potential gradient and aided by the unique smoothness of the carbon surface. The high thermal conductivity of the carbon composite membrane ensures that most of the latent heat is recovered.

The increasing imbalance between freshwater usage and available supply^{1–3} has led to water desalination becoming more important as a means of supplying freshwater to a thirsty world. Traditional desalination approaches involve either the process of distillation, which needs large amounts of energy, or the filtration approach using polymeric membranes, which need to have both a high salt rejection rate and a high freshwater flux. Most desalination units have adopted the energetically efficient reverse osmosis (RO) membrane process^{3,4}; however, membrane distillation (MD) and forward osmosis (FO) have also attracted intense attention in recent years⁵ because of their potential for integration with renewable energies. Among all of the filtration approaches, maintaining a high membrane flux constitutes a common challenge to all filtration approaches. A high flux membrane is highly desirable not only for reducing the membrane area but also for increasing productivity.

The polymeric membranes used in the RO and FO desalination processes function via the solution–diffusion mechanism; therefore, these membranes are necessarily dense. In contrast, membranes used in the MD process are microporous, whereby the hydrophobic micropores allow the transport of water vapour by Knudsen diffusion but block the transport of liquid. The flux in all of these polymeric membrane processes is limited by either the low permeability of the dense membrane structure or the low density of the transported water vapour. Recently, water was shown to transport superfast along aquaporin⁶ and carbon nanotube^{2,7–9} channels. A number of simulation studies^{10,11} have proposed that if the tube diameter is less than 1.1 nm, then salt can be effectively rejected through a molecular sieving mechanism. However, effective mechanisms for controlling the tube diameter and for sealing the gaps between tubes

remain a challenge in membrane fabrication. So, although aligned carbon nanotube layers have shown enhanced water flux^{12,13}, their application to water desalination has yet to be demonstrated. A common approach to sealing the gaps between tubes is to make mixed matrix membranes^{10,11,14–16}. Indeed, a commercial membrane made using this approach can achieve a high water flux of 7 litres per square metre per hour (LMH) in FO processes¹⁷. Meanwhile, a carbon nanotube–polyamide composite membrane was able to improve the specific water flux by a maximum of 3.6 LMH per bar in RO processes^{18,19}. However, the mixed matrix membrane approach suffers from many limitations, such as poor dispensability, low loading rate, improper alignment and defects. As a result, only limited success has been achieved when using this approach. Graphene and graphene oxide membranes have also shown potential in gas and liquid separations^{20–22}. In particular, when epoxy was used to encapsulate graphene oxide membranes to limit swelling effects, these membranes successfully rejected salt by up to 97%²³. However, these membranes are hard to scale-up and their real water flux values are still low.

Here, we report the synthesis of a nanoporous carbon composite membrane containing a layer of carbon fibres on a porous ceramic support; this composite membrane has a relatively open structure with a minimum pore size of ~30 nm. The membrane was successfully applied to RO, MD and FO membrane desalination processes and exhibited 100% salt rejection and a freshwater flux that was 3–20 times higher than those of existing polymeric membranes. Using a combination of vacuum membrane distillation (VMD), FO and energy accounting experiments, water was found to transport through the gaps of the carbon fibres. Molecular dynamics simulations revealed a novel interfacial salt sieving effect occurring in

¹Division of Physical Science and Engineering, King Abdullah University of Science and Technology, Thuwal, Saudi Arabia. ²CAS Key Laboratory of Low-Carbon Conversion Science and Engineering, Shanghai Advanced Research Institute, Chinese Academy of Sciences, Shanghai, China. ³Department of Physics, Hong Kong University of Science and Technology, Kowloon, Hong Kong, China. ⁴School of Astronautics, Northwestern Polytechnical University, Xi'an, China. ⁵Institute for Advanced Study, Hong Kong University of Science and Technology, Kowloon, Hong Kong, China.

*e-mail: zhiping.lai@kaust.edu.sa; sheng@ust.hk

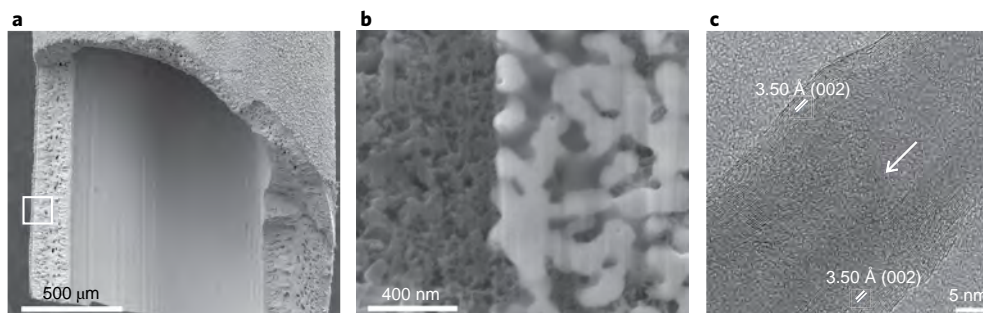


Fig. 1 | Structure of the membrane. **a**, Scanning electron microscopy (SEM) image of an as-prepared C-D35-2 membrane on the surface of a hollow YSZ tube. The square denotes the area that is magnified in **b**. **b**, An SEM with focused ion beam (FIB-SEM) image of the interface between the YSZ tube and the carbon layer. The interface between carbon and YSZ is clearly delineated. The nano-sized pores on the carbon side can also be seen. The pore size is smallest (~ 31 nm as determined by gas permeation analysis) in the vicinity of the carbon fibre–ceramic interface. **c**, HRTEM image of a typical single carbon nanofibre in the C-D35-2 membrane. The arrow indicates the bamboo-knot-like structure inside the carbon fibre that divides the interior space into compartments.

the membranes. This effect explained the high salt rejection rate of the composite membrane, and differs fundamentally from the solution–diffusion mechanism that occurs in polymeric membranes. This effect also differs from the molecular sieving mechanism that is expected to occur in carbon nanotubes and graphitic materials. Thus, desalination with a high freshwater flux and low energy consumption is achieved with the nanoporous carbon composite membrane owing to the relative smoothness and high thermal conductivity of its carbon surface accompanied by the nanoscale transport distance for Knudsen diffusion.

Membrane structure

Our carbon composite membrane was fabricated on a hollow yttrium-stabilized zirconia (YSZ) tube (Fig. 1a) with a porous wall. The obtained composite membrane is denoted as C-DP-X, where P denotes the nickel deposition power in Watts and X denotes the growth time in minutes.

The typical structure of the membrane is shown in Fig. 1. The thickness of the entire carbon layer is ~ 10 μm with a loose outer surface and a dense interface that separates the carbon layer and the YSZ support, as shown in Fig. 1b and by energy dispersive X-ray mapping analysis (see Supplementary Fig. 2). The effective region of the membrane, consisting of a dense growth of carbon fibres at the interface with the YSZ substrate, is only several hundreds of nanometres in thickness. The average pore size and porosity, as determined by gas permeation²⁴, are 31 nm and 22%, respectively. Detailed studies of numerous carbon fibres by high-resolution transmission electron microscopy (HRTEM), one image of which is shown in Fig. 1c, and Raman spectroscopy (Supplementary Fig. 3) revealed that every fibre studied exhibits a multiwall carbon nanotube structure. In contrast, the inner channels are always blocked by bamboo-knot-like structures, indicated by an arrow in Fig. 1c.

Liquid entry pressure and membrane distillation

Water cannot penetrate the nanoporous carbon membrane unless the applied pressure is higher than the liquid entry pressure (LEP). The measured LEPs for membranes with different pore sizes follow the relation $LEP = 4\gamma|\cos\theta|/(\text{pore size})$ (Supplementary Fig. 4), and a value of $\theta = 93^\circ$ was obtained by fitting the experimental LEP values with the simulated water–vapour interfacial tension of 58 mN m^{-1} (see below). Therefore, the nanoporous carbon membrane is equivalent to a porous (slightly) hydrophobic membrane that can be used for seawater desalination via membrane distillation.

Figure 2a shows the VMD setup, where a C-D35-2 membrane was immersed in a salt solution with one end sealed with epoxy resin and the other end connected to a vacuum pump through a condensation cold trap. The condensation cold trap can use either

liquid nitrogen or cold water at 2 °C, with the cold water achieving collection of only 1% less freshwater compared with the liquid nitrogen. NaCl solutions were used as synthetic seawater samples, and the salt concentrations were determined by measuring the conductivity at room temperature. In all experiments, the conductivity of the collected water after VMD was less than $2 \mu S cm^{-1}$, which is equivalent to 1 ppm salt concentration (that is, the salt rejection rate is over 99.99%). The freshwater fluxes of the C-D35-2 membrane at different temperatures and at different salinities of salt solutions are shown in Fig. 2b. The flux increased as the temperature increased, and above 40 °C, the water flux increased almost linearly with temperature. At 90 °C, approximately 1.34 litres of freshwater was collected from a 5 wt% NaCl solution after 48 h over a membrane area of $1.26 \times 10^{-4} m^2$, which gives a water flux of 221.6 LMH. Reducing the salinity of the feed solution increased the water flux to up to 413.5 LMH when fresh water was used as the feed solution. These values are substantially higher than the highest value reported for polymeric membranes operated in the direct contact mode, which is approximately 80 LMH²⁵. Moreover, these values are 15 to 20 times higher than that obtained using the non-contact mode, in which only vapour was in contact with the membrane. In Fig. 2b, the blue stars indicate the results obtained using the non-contact mode. For comparison, we show the water flux on a commercial polytetrafluoroethylene (PTFE) membrane (W.L. Gore) in the direct contact mode, which used the same setup as the results indicated as red open squares in the inset figure. The data match very well with the Knudsen diffusion predictions, with the absolute values in the range of 5 to 10 times lower than that of the nanoporous carbon membrane.

We attribute the high freshwater flux of the carbon membrane in the contact mode to the short Knudsen diffusion path. That is, salt solution can penetrate the loose carbon layer and stop at some specific location on the dense carbon layer due to the slight hydrophobicity of carbon. The vapour transport path is hence greatly reduced compared to the non-contact mode. The salt concentration polarization effect in our carbon composite membrane is strong because of the high flux, leading to a considerable decrease in the freshwater flux as the salinity of the feed solution increases. In contrast, the salt solution cannot enter polymeric membranes such as PTFE, polyvinylidene fluoride and polypropylene, which are often used in membrane distillation, owing to their strong hydrophobicity. Hence, even in the direct contact mode these polymeric membranes do not exhibit substantial differences with respect to the freshwater flux in the two modes, nor to the sensitivity on salinity.

We also conducted VMD desalination processes on seawater taken from the Red Sea, which has a salinity of 4.1%. Quantitative details are shown in Supplementary Figs. 7 and 8. Excellent desalination

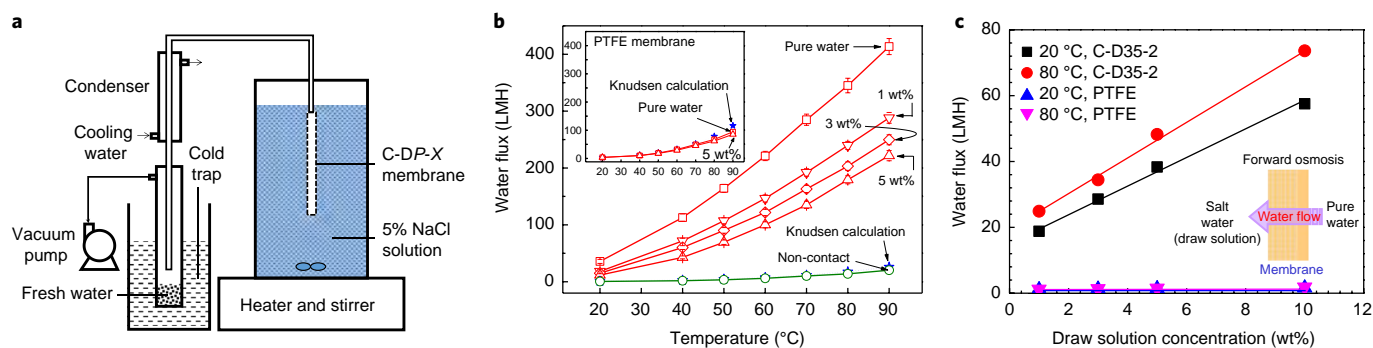


Fig. 2 | Freshwater transport through the C-D35-2 membrane. **a**, Schematic illustration of the VMD setup. **b**, The measured freshwater flux plotted as a function of temperature (red lines) at different salt concentrations. Blue stars denote the water flux predicted by Knudsen diffusion (labelled as Knudsen calculation), based on the measured data using methane gas, which has a similar molecular mass as water vapour. The green open circles denote the water flux in the non-contact mode when the membrane was exposed to only vapour (obtained by bubbling N_2 through water). The results are in good agreement with the Knudsen diffusion calculations. The inset shows the results over a PTFE membrane (pore size ~ 100 nm) in the direct contact mode, whereby the red lines are measured freshwater fluxes at different salt concentrations and the blue line is the calculated flux by Knudsen diffusion. **c**, The membrane freshwater flux in the FO process at two different temperatures (maintained to be the same on both sides of the membrane) plotted as a function of the draw solution salinity. The freshwater flux for the PTFE membrane is more than an order of magnitude lower. Inset: schematic illustration of the FO process.

performance was obtained (Supplementary Fig. 7), even though the freshwater flux is slightly lower compared to NaCl solutions with the same salinity. This difference is primarily attributed to the presence of divalent ions in seawater; divalent ions can reduce the water flux much more than monovalent ions²⁶. A similar reduction in the freshwater flux has been observed on commercial membranes^{27,28}. The scalability of our desalination approach was tested by using multiple membranes in parallel, and we found that the total flux was a linear function of the number of membranes (see Supplementary Section 4.2).

Forward and reverse osmosis

The inset in Fig. 2c illustrates the FO process, in which the membrane separates pure water from the salt solution, denoted the draw solution. The temperatures on both sides are maintained to be the same. Pure water diffuses across the membrane to the draw solution through vapour diffusion, driven by the chemical potential gradient. Figure 2c shows the FO water fluxes at different draw solution concentrations and at 20°C and 80°C. For comparison, we tested a commercial PTFE membrane in the same way and the results are denoted as star symbols in Fig. 2c. The magnitude of the water flux for the nanoporous carbon membrane was more than an order of magnitude higher than that of the PTFE membrane, and substantially higher than that for the commercial FO membranes, typically in the range between 5 and 10 LMH²⁹. Even when the salt ion concentration gradient was in the reverse direction, the salt leakage rate from the draw solution was almost zero. The salt concentration detected in the pure water stream was below 1 ppm during the 2 days of measurement, indicating that the salt rejection rate is higher than 99.9%.

A similar high freshwater flux was measured in the RO process (Supplementary Fig. 9a). A pressure of 3 bars, which is necessarily lower than the LEP of the membrane, was applied to the salt solution side. The salt solution was at the concentration of 2,000 ppm, which is in the brackish water salinity range. The applied pressure of 3 bars allowed the extraction of freshwater from salt solution. At 20°C, the specific water flux of the RO process was ~ 12 LMH per bar with a salt rejection rate of $\sim 100\%$. At 80°C, the specific water flux increased to 29 LMH per bar. Figure 9b shows the water flux as a function of the salt rejection trade-off diagram of existing membranes³⁰. Even at 20°C, the results show that the overall performance of the nanoporous carbon membrane is an order of magni-

tude better than any other membrane. As the applied pressure in the RO process should be higher than the osmotic pressure, the LEP of the C-D35-2 membrane, which is ~ 3.9 bar, would severely limit the application of this membrane to highly saline water. Below, we focus on energy accounting and theoretical modelling of the MD and FO processes, which have no such limitations arising from the LEP.

Energy accounting

Energy consumption constitutes a large proportion of the total desalination cost³. The composite carbon membrane showed high fluxes

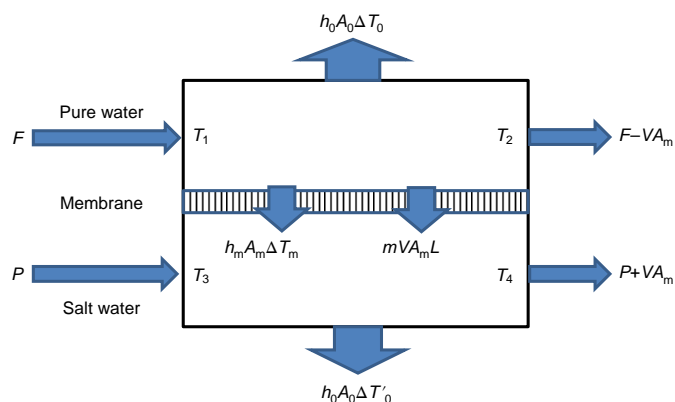


Fig. 3 | Energy accounting experiment. A schematic of the setup for measuring the temperature change of the desalination process. The terms $h_0 A_0 \Delta T_0$ and $h_0 A_0 \Delta T_0'$ represent the heat loss to the environment, where h_0 and A_0 are the module heat transfer coefficient and the surface area, respectively, and ΔT_0 and $\Delta T_0'$ are the average temperature difference between the streams and the environment at the feed and permeate side, respectively. The term $h_m A_m \Delta T_m$ represents the heat conduction between the two streams, where h_m and A_m are the membrane heat transfer coefficient and the membrane area, respectively, and ΔT_m is the average temperature difference between the two streams. F and P denote the constant flow rates of the pure water and salt water streams, respectively, and V is the transported freshwater flux from F to P . L is the latent heat of water and m is the percentage of water flux across the membrane that carries latent heat. The energy accounting measurements can yield the value of V and the energy consumption coefficient \bar{m} .

Table 1 | Ratio of the measured energy consumption over the theoretical latent heat consumption and the total freshwater flux

T_1 (°C)	C-D35-2 membrane		PTFE membrane	
	\bar{m} (%)	V (LMH)	\bar{m} (%)	V (LMH)
30	3	43.4	64	0.98
40	6	46.5	208	1.24
50	9	51.1	249	1.81
60	12	56.7	313	2.57
70	15	62.8	231	4.64
80	18	69.5	186	7.69

in all three of the membrane processes, a feature favourable for the possibility of integrating all three processes together to improve the flux. To study whether such an integration will be of benefit from an energy perspective, an energy accounting setup was designed, shown schematically in Fig. 3. One stream is fresh water and the other is salty water. The temperature of the fresh water is higher than that of the salty water. Hence, the entire process can be viewed as a combination

of the MD and FO processes. The temperature at the inlet and outlet of both streams were measured and denoted as T_1 , T_2 , T_3 and T_4 . The parameters h_0 and h_m shown in Fig. 3 are the heat transfer coefficients to account for the heat loss to the environment and the heat conduction between the two streams, respectively. The values of h_0 at different temperatures were determined using a separate experiment, in which an impermeable membrane was used (see Supplementary Section 5.1). From the temperature data, the measured in-flow and out-flow rates P and F , respectively, and the membrane flux V on the two sides of the membrane, plus the known values of latent heat and specific heats of water, an energy consumption coefficient \bar{m} , defined as the ratio of the measured energy consumption over the theoretical latent heat consumption, can be obtained (see Supplementary Section 5.2). The results, listed in Table 1, show that \bar{m} increases with T_1 , but even at 80 °C, only ~10–20% of the theoretical latent heat is consumed. However, when a PTFE membrane was used, $\bar{m} > 100\%$ for temperatures over 30 °C. These results are consistent with the data shown in Fig. 2b. These results also indicate that the intrinsic energy consumption of this process (FO plus a temperature gradient) is reduced by at least 80% in the nanoporous carbon membrane compared to the PTFE membrane. Table 1 also shows the order of magnitude difference in the transported freshwater fluxes between the two membranes.

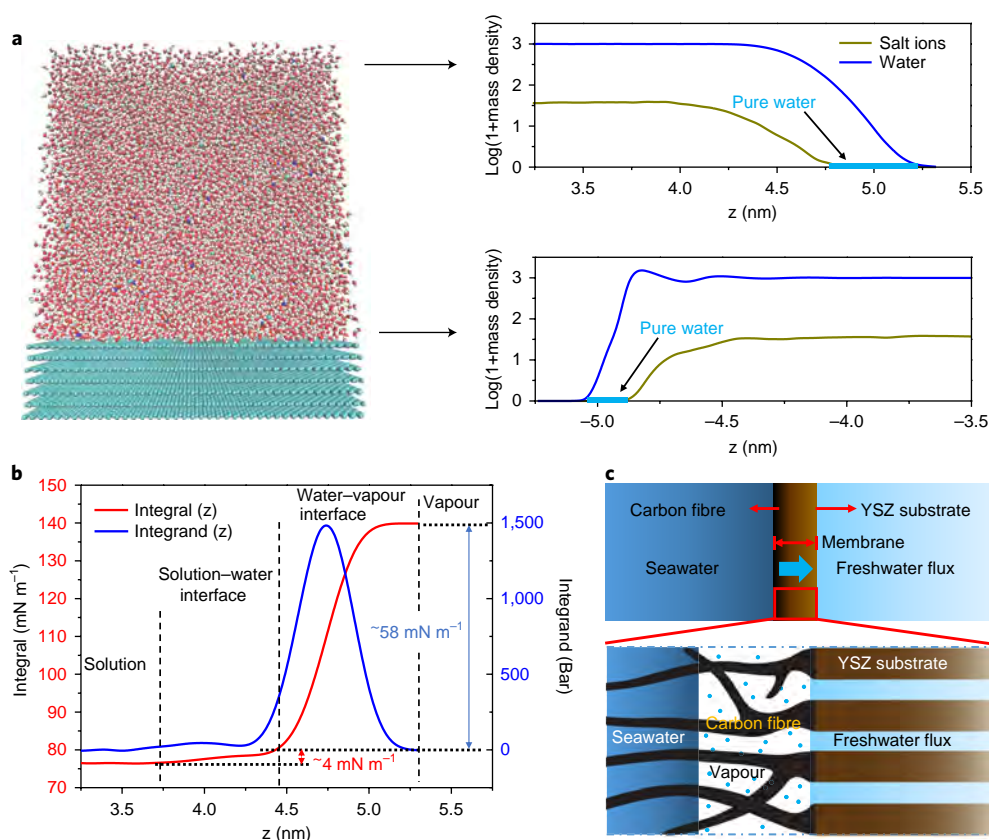


Fig. 4 | Desalination mechanism. **a**, Left: a molecular view of the simulated system. The concentration of the salt solution is ~3.5 wt%. Right: top figure shows the densities of salt ions (green line) and the water (blue line). Mass density is in units of g per litre. Two to three atomic layers of pure water are seen at the water–vapour interface, indicated by the light blue line. The lower figure shows the same at the carbon–salt solution interface. A monolayer of pure water exists at the carbon surface. The surface water layer is noted to have a lower density than the bulk. The centre of the first carbon atomic layer is located at -5.35 nm. So, there is a small ‘air gap’ of ~ 3 Å. **b**, The blue line indicates the anisotropic component of the stress tensor, for which the integral (red line) gives the surface tensions. In addition to the water–vacuum interfacial tension of 58 mN m $^{-1}$, there is a small interfacial tension between pure water and the saline solution that prevents mixing of the salt ions with the surface water layer. **c**, Vapour diffusion and the interfacial salt sieving effect. The bottom panel is a magnified illustration of the dense section of the carbon membrane closest to the YSZ substrate. It shows two menisci separated by a gap in which rapid water vapour transport through Knudsen diffusion takes place. An explanation of the freshwater transport process is provided in the main text.

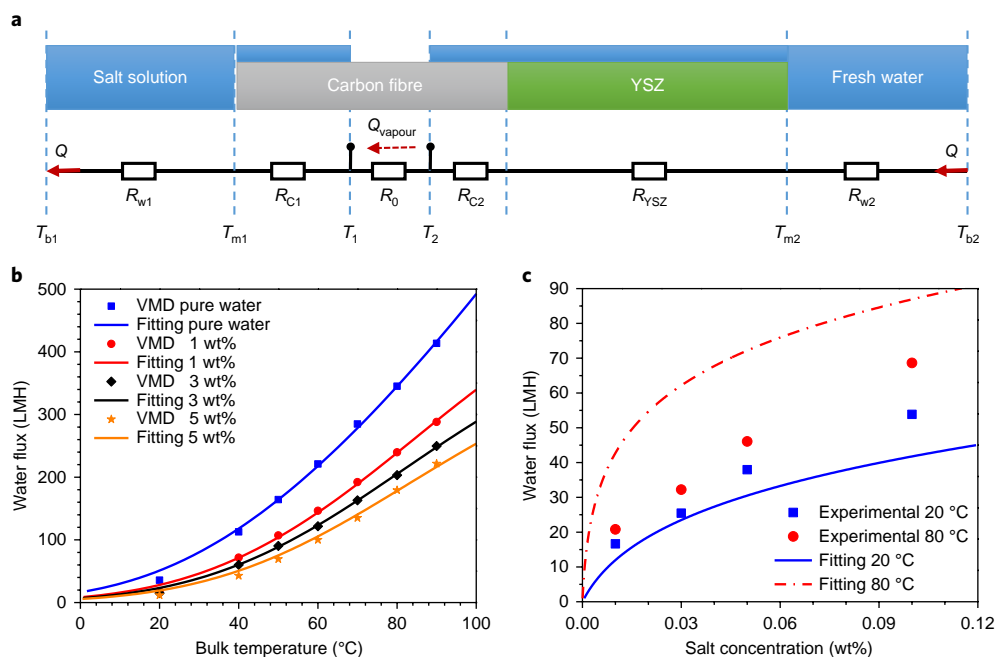


Fig. 5 | Predicted heat and mass transport by theoretical modelling and MD simulations in the carbon composite membrane. a, A resistance-in-series model to predict the transport through the carbon composite membrane. In the model, R represents thermal resistance of each part, Q denotes the heat flux and T is temperature at different positions. **b**, Freshwater flux in the VMD experiment plotted as a function of temperature. The symbols represent experimental results, the curves represent the theoretical fit (see below and Supplementary Section 6.3). **c**, Freshwater flux in the FO experiment plotted as a function of the salt concentration of the draw solution. Blue and red symbols are experimental results at 20 °C and 80 °C, respectively, while the blue and red curves are the theoretical predictions at 20 °C and 80 °C, respectively. The nonlinear behaviour seen in both the experimental data and the theoretical results is the manifestation of the concentration polarization effect.

Desalination mechanism

It is clear from the LEP studies that because the nanoporous carbon membrane is slightly hydrophobic, a meniscus will necessarily be formed on the feed side. During the RO and FO processes, another meniscus will be formed on the permeate side. The two menisci are separated by a gap. Such a microstructure is completely different from that of the dense polymeric membranes. To clarify the mechanism for the three salient features (high salt rejection rate, high flux and low energy consumption) of the carbon composite membrane, we performed large-scale molecular dynamics simulations on the water vapour transport characteristics in the vicinity of the menisci and the gap in between. The simulations primarily focused on two aspects: the salt distribution near the menisci (Fig. 4a,b) and the dynamic transport of water molecules in the gap between the two menisci (Fig. 4c, and detailed below as well as in Supplementary Sections 6 and 7).

The simulation results (Fig. 4b) indicate that there is a small interfacial tension, $\sim 4 \text{ mN m}^{-1}$, between pure water and the saline solution that prevents mixing of the salt ions with the surface water layer. As a consequence, as illustrated in Fig. 4a, there is a thin layer between the salt water and the carbon surface, as well as between the salt water and its vapour, containing no salt. This interfacial salt sieving effect is the same as the formation of solvation shells, in which each salt ion is enveloped by a layer of structured water molecules^{31,32}. This effect prevents the salt ions from being in direct contact with the water–vapour or the graphitic interface³³, at which water molecules also form the layered structures³⁴. For a salt ion to leave the meniscus, it has to either exit the solvation shell or bring the entire solvation cluster with it. In both scenarios, the energy required is prohibitively high. The molecular dynamics simulation also showed that water vapour can rarely condense to form stable droplets on the carbon surface owing to the relatively large pore size ($\sim 30 \text{ nm}$) and the slight hydrophobicity of the carbon surface, as well as the sub-saturated or near-saturated vapour environment in the

MD or FO/RO process. This effect excludes the possibility of surface diffusion of water droplets. Hence, the freshwater flux through the carbon composite membrane is due to vapour transport, and the salt rejection mechanism is no different from the evaporation process.

We used a resistance-in-series model to simulate the water flux in the FO and VMD processes, as well as the energy consumption in the energy accounting experiment. Figure 5a shows a schematic of the model. For the energy accounting experiment, the net heat flux Q has the following relationship with the latent heat flux Q_{vapour} ,

$$Q = \frac{R_0}{\sum R_i} Q_{\text{vapour}} + \frac{T_{b2} - T_{b1}}{\sum R_i} \quad (1)$$

where R_i is the thermal resistance of each part, and T_{b1} and T_{b2} are the temperatures of the bulk streams on the two sides indicated in Fig. 5. The factor before Q_{vapour} is less than 2×10^{-7} because of the low thermal resistance of the carbon fibres between the two menisci R_0 (see Supplementary Section 6.1). Hence, the net heat flux Q measured in the experiment is not sensitive to the latent heat flux Q_{vapour} . If the vapour transport flux is large, Q_{vapour} can be much larger than the net heat flux Q . In that case, most of the Q_{vapour} is recovered through the carbon fibres between the two menisci.

From the molecular dynamics simulations, the transport resistance of vapour across the gap between the two menisci was obtained (see Supplementary Section 7); this value was much lower than that predicted using an analytical model³⁵ developed under the assumptions of diffuse vapour–surface scattering and Hertz relation. This discrepancy is attributed to the following two aspects: the unique smooth surface of the carbon pore and the non-equilibrium state of vapour in the narrow gap (see Supplementary Section 7). These findings are in agreement with many other simulation studies of the transport in graphitic materials^{36–38}. The high water flux will therefore induce a concentration

polarization effect at the menisci, which limits the overall flux. After considering the concentration polarization effect, the predicted VMD and FO water fluxes were plotted and compared with experimental results (Fig. 5b,c, see also Supplementary Sections 6.2 and 6.3 for details). The results of the VMD agree well with the experimental results, and reveal that the salinity-dependent flux is due to the concentration polarization effect, when ions need to diffuse from the menisci to the bulk streams. The predicted flux of FO at 20°C also matches well with the experimental results, which suggests that even at room temperature, the mechanism of vapour transport can yield a relatively high flux. However, the predicted flux at 80°C is higher than the experimental result, indicating that the flow is severely limited by the concentration polarization effect.

Conclusions

In summary, a nanoporous carbon composite membrane displayed unprecedented high water flux in three membrane-based desalination processes. The large freshwater flux is attributed to the rapid transport of water vapour through nano-sized carbon pores, while the excellent salt rejection rate is attributed to the interfacial sieving effect. This high flux desalination mechanism, with latent heat recovery, opens the possibility of considerable energy savings for the desalination process, and the FO process combined with a temperature gradient is a promising direction for its realization.

Methods

Methods, including statements of data availability and any associated accession codes and references, are available at <https://doi.org/10.1038/s41565-017-0040-8>.

Received: 28 September 2015; Accepted: 17 January 2018;

Published online: 05 March 2018

References

- Elimelech, M. & Phillip, W. A. The future of seawater desalination: energy, technology and the environment. *Science* **333**, 712–717 (2011).
- Shannon, M. A. et al. Science and technology for water purification in the coming decades. *Nature* **452**, 301–309 (2008).
- Cipollina, A. et al. (eds) *Seawater Desalination* (Springer, Heidelberg, 2009).
- Ghaffour, N., Missimer, T. M. & Amy, G. L. Technical review and evaluation of the economics of water desalination: Current and future challenges for better water supply sustainability. *Desalination* **309**, 197–207 (2013).
- El-Ghonemy, A. M. K. Water desalination systems powered by renewable energy sources: Review. *Renew. Sust. Energy Rev.* **16**, 1537–1556 (2012).
- Kumar, M., Habel, J. E. O., Shen, Y. X., Meier, W. P. & Walz, T. High-density reconstitution of functional water channels into vesicular and planar block copolymer membranes. *J. Am. Chem. Soc.* **134**, 18631–18637 (2012).
- Holt, J. K. et al. Fast mass transport through sub-2-nanometer carbon nanotubes. *Science* **312**, 1034–1037 (2006).
- Theresa, M., Pendergast, M. & Hoek, M. V. A review of water treatment membrane nanotechnologies. *Energy Environ. Sci.* **4**, 1946–1971 (2011).
- Verweij, H., Schillo, M. C. & Li, J. Fast mass transport through carbon nanotube membranes. *Small* **3**, 1996–2004 (2007).
- Song, C. & Corry, B. Intrinsic ion selectivity of narrow hydrophobic pores. *J. Phys. Chem. B* **113**, 7642–7649 (2009).
- Corry, B. Water and ion transport through functionalised carbon nanotubes: implications for desalination technology. *Energy Environ. Sci.* **4**, 751–759 (2011).
- Srivastava, A., Srivastava, O. N., Talapatra, S., Vajtai, R. & Ajayan, P. M. Carbon nanotube filters. *Nat. Mater.* **3**, 610–614 (2004).
- Tofi hy, M. A., Shirazi, Y., Mohammadi, R. & Park, A. Salty water desalination using carbon nanotubes membrane. *Chem. Eng. J.* **168**, 1064–1072 (2011).
- Majumder, M. & Ajayan, P. M. in *Comprehensive Membrane Science and Engineering* (eds E. Drioli & L. Giorno) 291–310 (Elsevier, UK, 2010).
- Mi, W. L., Lin, Y. S. & Li, Y. D. Vertically aligned carbon nanotube membranes on macroporous alumina supports. *J. Membr. Sci.* **304**, 1–7 (2007).
- Kim, S., Jinschek, J. R., Chen, H., Sholl, D. S. & Marand, E. Scalable fabrication of carbon nanotube/polymer nanocomposite membranes for high flux gas transport. *Nano Lett.* **7**, 2806–2811 (2007).
- Zhong, Y. J. et al. Using UCST ionic liquid as a draw solute in forward osmosis to treat high-salinity water. *Environ. Sci. Technol.* **50**, 1039–1045 (2016).
- Ratto, T. V., Holt, J. K. & Szmodis, A. W. Membranes with embedded nanotubes for selective permeability. US patent 7,993,524 (2011).
- Lee, H. D., Kim, H. W., Cho, Y. H. & Park, H. B. Experimental evidence of rapid water transport through carbon nanotubes embedded in polymeric desalination membranes. *Small* **10**, 2653–2660 (2014).
- Nair, R. R., Wu, H. A., Jayaram, P. N., Grigorieva, I. V. & Geim, A. K. Unimpeded permeation of water through helium-leak-tight graphene-based membranes. *Science* **335**, 442–444 (2012).
- Joshi, R. K. et al. Precise and ultrafast molecular sieving through graphene oxide membranes. *Science* **343**, 752–754 (2014).
- Kim, H. W. et al. Selective gas transport through few-layered graphene and graphene oxide membranes. *Science* **342**, 91–95 (2013).
- Abraham, J. et al. Tunable sieving of ions using graphene oxide membranes. *Nat. Nanotech.* **12**, 546–551 (2017).
- Yasuda, H. & Tsai, J. T. Pore size of microporous polymer membranes. *J. Appl. Polym. Sci.* **18**, 805–819 (1974).
- Wang, P., Teoh, M. M. & Chung, T. S. Morphological architecture of dual-layer hollow fiber for membrane distillation with higher desalination performance. *Water Res.* **45**, 5489–5500 (2011).
- Fornasiero, F. et al. Ion exclusion by sub-2-nm carbon nanotube pores. *Proc. Natl Acad. Sci. USA* **105**, 17250–17255 (2008).
- Schaepe, J., Vandecasteele, C., Mohammad, A. W. & Bowen, W. R. Modelling the retention of ionic components for different nanofiltration membranes. *Sep. Purif. Technol.* **22–23**, 169–179 (2001).
- Peeters, J. M. M., Boom, J. P., Mulder, M. H. V. & Srahtmann, H. Retention measurements of nanofiltration membranes with electrolyte solutions. *J. Membr. Sci.* **145**, 199–209 (1998).
- Chekli, L. et al. A comprehensive review of hybrid forward osmosis systems: performance, applications and future prospects. *J. Membr. Sci.* **497**, 430–449 (2016).
- Geise, G. M., Park, H. B., Sagle, A. C., Freeman, B. D. & McGrath, J. E. Water permeability and water/salt selectivity tradeoff in polymers for desalination. *J. Membr. Sci.* **369**, 130–138 (2011).
- Dang, L. X., Rice, J. E., Caldwell, J. & Kollman, P. A. Ion solvation in polarizable water: molecular dynamics simulations. *J. Am. Chem. Soc.* **113**, 2481–2486 (1991).
- Mancinelli, R., Botti, A., Bruni, F., Ricci, M. A. & Soper, A. K. Hydration of sodium, potassium, and chloride ions in solution and the concept of structure maker/breaker. *J. Phys. Chem. B* **111**, 13570–13577 (2007).
- Taherian, F., Marcon, V., van der Vegt, N. F. A. & Leroy, F. What is the contact angle of water on graphene? *Langmuir* **29**, 1457–1465 (2013).
- Kimmel, G. A. et al. No confinement needed: observation of a metastable hydrophobic wetting two-layer ice on graphene. *J. Am. Chem. Soc.* **131**, 12838–12844 (2009).
- Lee, J. & Karnik, R. Desalination of water by vapor-phase transport through hydrophobic nanopores. *J. Appl. Phys.* **108**, 044315 (2010).
- Skoulidas, A. I., Ackerman, D. M., Johnson, J. K. & Sholl, D. S. Rapid transport of gases in carbon nanotubes. *Phys. Rev. Lett.* **89**, 185901 (2002).
- Arya, G., Chang, H.-C. & Maginn, E. Knudsen diffusivity of a hard sphere in a rough slit pore. *Phys. Rev. Lett.* **91**, 026102 (2003).
- Falk, K., Sedlmeier, F., Joly, L., Netz, R. R. & Bocquet, L. Molecular origin of fast water transport in carbon nanotube membranes: superlubricity versus curvature dependent friction. *Nano Lett.* **10**, 4067–4073 (2010).

Acknowledgements

Commercial PTFE membranes and FO membranes were provided by N. Ghaffour and T. Zhang from the KAUST Water Desalination and Reuse Center. Z.L. acknowledges support from KAUST (grant URF/1/1723) and KACST (grant RGC/3/1614). P.S. acknowledges support from KAUST (Special Partnerships Award number UK-C0016 and grant SA-C0040), HKUST (grant SRFI 11/SC02) and the William Mong Institute of Nanoscience and Technology (grant G5537-E).

Author contributions

Z.L. and W.C. conceived the initial ideas and experimental design. S.C., T.L. and P.S. contributed to the desalination mechanism and the relevant simulations and data analyses. W.C., Q.Z., Z.F. and H.Y. carried out the experiments, and T.L. and S.C. carried out the MD simulations. K.-W.H. contributed to data analyses, and X.Z. contributed to characterization and data analyses. Z.L., W.C. and P.S. wrote the first draft, and Z.L., W.C., P.S., S.C., T.L. and X.Z. participated in the revisions.

Competing interests

The authors declare no competing interests.

Additional information

Supplementary information is available for this paper at <https://doi.org/10.1038/s41565-018-0067-5>.

Reprints and permissions information is available at www.nature.com/reprints.

Correspondence and requests for materials should be addressed to Z.L. or P.S.

Publisher's note: Springer Nature remains neutral with regard to jurisdictional claims in published maps and institutional affiliations.

Methods

Experimental. *Growth of carbon nanostructures on the hollow fibre.* YSZ hollow fibres were custom-made from YSZ nanoparticles (30–60 nm from Inframat Advanced Materials Co.) through a phase-inversion and sintering process^{39,40}. The diameter of the YSZ hollow fibre was ~0.91 mm with an average pore size of 100 nm and porosity of 40%. The outer surface of the YSZ hollow fibres was uniformly coated with nickel nanoparticles (20–30 nm, Supplementary Fig. 1c) using a rotational sputtering deposition method. A carbon layer was grown on the nickel-deposited YSZ hollow fibres through a catalytic chemical vapour deposition (CVD) process, in which acetylene was used as the carbon source in the presence of hydrogen gas (acetylene to hydrogen volume ratio 1:10) to grow carbon nanowires at 700 °C for 1–3 min. Then, the CVD chamber was quickly cooled down to room temperature under argon flow. A carbon composite membrane can also be grown on a YSZ flat-sheet support following the same procedure.

Membrane characterization. Raman spectroscopy measurements of the outer surface of the carbon composite membranes were carried out on a Horiba Aramis confocal microprobe Raman instrument equipped with a He–Ne laser ($\lambda = 632.8$ nm). SEM images were taken using a FEI Nova Nano630 equipped with a focused ion beam (FIB), which facilitates the acquisition of an ultrasmooth interface of carbon composite membrane while preserving the initial structure. The elemental distributions of the membrane were analysed by energy dispersive X-ray mapping in SEM. TEM images were obtained using a Titan ST microscope (FEI Co.) operating at 300 kV.

Energy accounting experiment. Carbon composite membranes grown on YSZ flat-sheet supports were used for energy accounting experiments because a large space was required to house the temperature probes on both sides of the membrane. Commercial porous PTFE membranes (W.L. Gore) and dense polyethylene sheets were used as references for comparison. The membranes were mounted into a permeation cell made of polymethyl methacrylate. Fresh water and draw solution (10 wt% NaCl) were recycled in each side of the membrane through circulation bathes. At each measurement point, the experiment was run for ~5 h to reach steady state, then the weight, conductivity and temperatures at the inlet and outlet of each stream were recorded.

Theory. *Molecular dynamics simulations.* Molecular dynamics simulations were carried out using the package GROMACS 4.6.7 (ref. 41). Parameterized force fields were adopted to describe the atomic interactions in the system^{42–44}.

The concentration of the NaCl solution was set to ~3.5 wt%, similar to that of seawater. Carbon atoms were fixed at the crystallographic positions of the graphite lattice. All bonds of water molecules were constrained using the SHAKE method⁴⁵. Simulations showing the salt rejection mechanism were performed for 5 ns in the canonical ensemble with Berendsen thermostat⁴⁶ at a constant temperature of 300 K. The time step was set to be 1 fs. Long-range electrostatic interactions were calculated with the particle mesh Ewald technique⁴⁷ and the van der Waals interactions were cut off at 1.2 nm. A custom GROMACS version based on GROMACS 4.5.5 was used to compute the 3D stress tensor from the simulated data⁴⁸.

References

- Liu, S. M., Li, K. & Hughes, R. Preparation of porous aluminium oxide (Al₂O₃) hollow fibre membranes by a combined phase-inversion and sintering method. *Ceram. Int.* **29**, 875–881 (2003).
- Wang, B. & Lai, Z. P. Finger-like voids induced by viscous fingering during phase-inversion of alumina/PES/NMP suspensions. *J. Membr. Sci.* **405–406**, 275–283 (2012).
- Van Der Spoel, D. et al. GROMACS: fast, flexible, and free. *J. Comp. Chem.* **26**, 1701–1718 (2005).
- Weerasinghe, S. & Smith, P. E. A Kirkwood–Buff derived force field for sodium chloride in water. *J. Chem. Phys.* **119**, 11342–11349 (2003).
- Werder, T., Walther, J. H., Jaffe, R., Halicioglu, T. & Koumoutsakos, P. On the water–carbon interaction for use in molecular dynamics simulations of graphite and carbon nanotubes. *J. Phys. Chem. B* **107**, 1345–1352 (2003).
- Oostenbrink, C., Villa, A., Mark, A. E. & van Gunsteren, W. F. A biomolecular force field based on the free enthalpy of hydration and solvation: the GROMOS force-field parameter sets 53A5 and 53A6. *J. Comp. Chem.* **25**, 1656–1676 (2004).
- Ryckaert, J. P., Ciccotti, G. & Berendsen, H. J. Numerical integration of the Cartesian equations of motion of a system with constraints: molecular dynamics of n-alkanes. *J. Comp. Phys.* **23**, 327–341 (1977).
- Berendsen, H. J., Postma, J. P. M., van Gunsteren, W. F., DiNola, A. & Haak, J. Molecular dynamics with coupling to an external bath. *J. Chem. Phys.* **81**, 3684–3690 (1984).
- Essmann, U. et al. A smooth particle mesh Ewald method. *J. Chem. Phys.* **103**, 8577–8593 (1995).
- Vanegas, J. M., Torres-Sánchez, A. & Arroyo, M. Importance of force decomposition for local stress calculations in biomembrane molecular simulations. *J. Chem. Theory Comput.* **10**, 691–702 (2014).